



Milling mechanism and surface roughness prediction model in ultrasonic vibration-assisted side milling of Ti–6Al–4 V

Weiwei Ming¹ · Chongyan Cai¹ · Zheng Ma¹ · Ping Nie^{2,3} · Changhe Li⁴ · Qinglong An¹

Received: 12 January 2023 / Accepted: 12 February 2023 / Published online: 27 February 2023
© The Author(s), under exclusive licence to Springer-Verlag London Ltd., part of Springer Nature 2023

Abstract

Ultrasonic vibration-assisted (UVA) cutting is an advanced technique to improve the machinability and productivity of difficult-to-machine materials. This paper aims to assess the cutting performance of ultrasonic vibration-assisted milling (UVAM) technique and conventional milling (CM) in side milling of Ti–6Al–4 V. Tool trajectory and instantaneous chip thickness are calculated considering tool runout, vibration, and deflection. The geometric-kinematic-dynamic surface topography matrix and its corresponding material elastic recovery height matrix are reconstructed based on tool trajectory and cutting thickness, which are then summed to obtain the geometric-kinematic-dynamic-physical surface topography matrix. Finally, roughness parameters R_a and R_z are predicted based on the final reconstructed physical surface topography matrix. Experimental results show that R_a and R_z of UVAM are on average 26 and 39% greater, respectively, compared to CM due to the presence of high-frequency ultrasonic vibration-induced texture patterns in the feed grooves. The average prediction error for R_a and R_z is 23%, proving the validity of the prediction model. UVAM reduces the radial and tangential cutting force coefficients and ploughing force coefficients compared to CM due to the separation and impact effect of ultrasonic vibration. However, UVAM leads to an increase in the axial ploughing force coefficient because ultrasonic vibration introduces relative motion and friction between the tool and the workpiece in the axial direction.

Keywords Ultrasonic vibration · Surface roughness · Side milling · Ti–6Al–4 V · Milling force coefficients

1 Introduction

Ultrasonic vibration-assisted (UVA) machining is an advanced manufacturing technology that causes the tool or workpiece to vibrate during machining, where the amplitude is typically within a few microns and the frequency is typically greater than 20 kHz [1]. For example, UVA machining

has been applied to hard-to-machine metallic material [2, 3], ceramic material [4], carbon fiber-reinforced plastic (CFRP) [5–8], metal matrix composite [9, 10], ceramic matrix composite [11], etc., to improve their machinability. Another effect of ultrasonic vibration is to improve the stability of milling system [12]. Titanium alloys are widely used in aircraft engines and medical devices because of their high specific strength, corrosion resistance, and biocompatibility [13]. However, they are difficult to machine because, for example, cutting temperatures are high, so the material tends to spring back, and tools are prone to wear [14, 15]. Luckily, ultrasonic vibration offers the potential to improve the machinability and productivity of titanium alloys. Machined surface roughness affects the mechanical and service performance of parts [16, 17]. Therefore, it is significant to study the cutting mechanism and roughness during UVA machining of titanium alloys.

An important benefit of UVA machining is reduction in cutting forces [18] or grinding forces [19]. This reduction is due to the transformation of continuous chips into broken small chips by high-frequency vibration [20], the

✉ Ping Nie
nieping@alumni.sjtu.edu.cn

¹ School of Mechanical Engineering, Shanghai Jiao Tong University, Shanghai 200240, People's Republic of China

² Department of Oral and Cranio-Maxillofacial Surgery, Shanghai Ninth People's Hospital, Shanghai Jiao Tong University School of Medicine, Shanghai 200011, People's Republic of China

³ College of Stomatology, Shanghai Jiao Tong University, Shanghai 200240, People's Republic of China

⁴ School of Mechanical and Automotive Engineering, Qingdao University of Technology, Qingdao 266520, People's Republic of China

acceleration of chips [21], and the reduction of contact length [19]. Feng et al. [22] investigated three types of tool-to-workpiece separation criteria for ultrasonic vibration-assisted milling (UVAM) based on tool path. The actual contact time (or duty cycle) between tool and workpiece is a key parameter in determining the intermittent cutting characteristics during UVA turning [23] and UVA milling [24]. Ni et al. [24] developed an analytical model to calculate duty cycle during UVAM. They found that milling forces decreased with increasing ultrasonic amplitude due to the reduced net cutting time. Jung et al. [25] found that ultrasonic vibration increased the cutting width and reduced the average undeformed cutting thickness, thus reducing the forced vibration due to serrated chips and hence the milling force of Ti–6Al–4 V. Lotfi et al. [26] investigated the milling forces in UVAM of CFRP and titanium and found that the milling forces were reduced in both the feed and vertical feed directions; however, the axial forces increased as the ultrasonic vibration caused additional tool motion in the axial direction. Greco et al. [27] found that ultrasonic vibrations reduced milling forces and burr generation during micro-milling of 3D printed AISI 316L. Wear of tools or grinding wheels under ultrasonic vibration-assisted machining is also a topic of interest for scholars. Cao et al. [28] developed a wear volume prediction model for grinding wheel in UVA grinding. Sorgato et al. [29] found that tool wear under UVA drilling conditions was less than that under conventional drilling condition only at low feed rates; the opposite was true at high feed rates.

In addition to using ultrasonic vibration technology alone to improve material machinability, ultrasonic vibration can be combined with minimal-quantity lubrication technology to refine droplets and promote droplet penetration into the cutting zone, reducing surface roughness relative to conventional milling, advantages that have been observed in milling Ti6Al4V [30], milling Al6061-T6 [31], and grinding GH4169 nickel-based alloy [32].

An additional role of UVA cutting is the creation of functional surfaces with special textures [33] to improve the wear resistance and reduce the friction coefficient of the part surface [34, 35]. For example, Börner et al. [36] proposed to incorporate ultrasonic vibrations in face milling to generate the desired functional surface microstructure and proposed a method to simulate the functional surface topography based on tool kinematic trajectory and tool geometry. Chen et al. [37] simulated the surface texture of machined floor surface after UVA micro-milling based on a tool edge sweep technique, taking into account ideal tool path and tool geometry.

Regarding the roughness in UVAM, Chen et al. [38] observed a lower roughness in UVAM compared to conventional milling (CM) with ball-end mill. Zhao et al. [39] reported the dependence of surface roughness on the ultrasonic amplitude. However, other scholars have found that

ultrasonic vibration increases machined surface roughness [40–42]. For example, Zhang et al. [41] found that although ultrasonic vibration suppressed sticky chips on the floor surface, the introduction of a ridged texture led to an increase in roughness. Maurotto and Wickramarachchi [42] found that ultrasonic vibration resulted in finer and more uniform textures on the milled surface but increased roughness, and that the roughness increased with increasing ultrasonic frequency. Although there have been many studies on the end-milled floor surface roughness in UVAM, there are few studies on the quantitative prediction of roughness during UVA side milling of Ti–6Al–4 V.

During side milling, tool runout [43–46], forced vibrations [47–50], self-excited vibration (chatter) [51–53], and tool wear [54, 55] can largely affect the roughness of the machined side surface, and static tool deflection affects the surface topography mainly on the form error scale [56]. Material springback effects need to be considered in micro-milling process [57]. Arizmendi et al. [58] developed an analytical model of the equivalent tool rotation radius in the presence of tool setting error. Later, Arizmendi et al. [59] proposed a method to identify tool setting error based on the analysis of surface topography. Later, Arizmendi et al. [60] added the tool grinding error into the surface roughness prediction model. Niu et al. [61] developed a prediction model for the surface profile in milling with variable pitch end mill. Artetxe et al. [62] developed a predictive model for 3D surface topography of side-milled thin-walled parts, taking into account tool setting error, workpiece deflection, and radial cutting width variations. The machining of complex parts requires the use of tools with complex geometries, for example, for inclined milling operations using circle-segment end mills, Urbikain and López de Lacalle [63] developed a predictive model for surface topography that takes into account tool geometry, milling parameters, tool orientation angles, and tool runout, and in the future, this model could be upgraded by introducing a milling force model proposed by Urbikain Pelayo [64] to include the effect of vibration displacements in surface topography. Subsequently, Urbikain Pelayo et al. [65] developed a geometric model of surface roughness for side milling operations using barrel-shaped mills, considering tool geometry and variation of tool runout values along axial direction.

Although there has been extensive research on machined surface profile in CM, there has been less research on surface roughness and milling force coefficients for UVA side milling of Ti–6Al–4 V. Therefore, in this paper, the instantaneous trajectory and cutting thickness of each tooth and each axial slice of end mill were calculated, considering cutter geometry, tool runout and ideal tool trajectory (geometric-kinematic factors), and tool deflection and vibration induced by milling forces (dynamic factors). Then, the geometric-kinematic-dynamic surface topography matrix

and the corresponding uncut chip thickness matrix were reconstructed. The material elastic recovery height was then calculated based on uncut chip thickness. The geometric-kinematic-dynamic surface topography matrix and the material elastic recovery height matrix were then summed to obtain the physics-based surface topography matrix, from which the roughness parameters R_a and R_z were finally predicted. The roughness prediction model was validated by UVA side milling experiments on Ti–6Al–4 V. In addition, the average milling forces and milling force coefficients were also analyzed.

2 Cutting mechanism of UVAM

The features of UVAM are related to tool trajectory, cutting thickness and equivalent cutting speed. It is therefore necessary to study them first. The schematic diagram of UVA side milling is illustrated in Fig. 1(a). The cutter vibrates at a high frequency in the axial, feed, and vertical feed directions. Figure 1(b) shows the cross-section of end mill. According to the coordinate system established in Fig. 1(b), the trajectory of tool tip can be expressed by the following equation:

$$\begin{aligned} x(i, j, k) &= -R\sin(\phi_{i,j,k}) + A_x\cos(2\pi ft + \theta_x) - v_f t \\ y(i, j, k) &= -R\cos(\phi_{i,j,k}) + A_y\cos(2\pi ft + \theta_y) \\ z(i, j, k) &= z_j + A_z\cos(2\pi ft + \theta_z) \end{aligned} \quad (1)$$

where i is the index of differential element of tool rotation angle, j is the index of axial micro-disk layer of tool, k is tooth index, and z_j is height for j^{th} axial slice. R is nominal cutter radius. $\phi_{i,j,k}$ is the instantaneous immersion angle for k^{th} tooth and j^{th} axial slice at the moment t_i . v_f is the feed speed (in mm/min). A_x , A_y , and A_z are ultrasonic vibration amplitudes. f is ultrasonic vibration frequency. θ_x , θ_y , and θ_z are phases.

The feed speed v_f is expressed by the following equation:

$$v_f = N_t f_t n \quad (2)$$

where N_t is tooth number, f_t is feed per tooth (in mm/tooth/rev), and n is spindle speed.

The instantaneous immersion angle $\phi_{i,j,k}$ is given by

$$\phi_{i,j,k} = \omega t - (k - 1)\phi_p - \frac{\tan \beta}{R} z_j \quad (3)$$

where ω is the angular velocity of tool (in rad/s, and $\omega = 2\pi n$). ϕ_p is pitch angle, and $\phi_p = 2\pi/N_t$. β is helix angle.

Figure 2 depicts the trajectory of tool tip during UVAM. It can be noticed that the tool tip trajectory has a return process, signifying the high-frequency separation of tool-chip and tool-workpiece. The tool tip trajectory in CM is a trochoid and the tool does not move back and forth, thus there is no high-frequency separation effect. The instantaneous cutting thickness in UVAM can be calculated numerically, as shown in Fig. 2. At the moment of rotation angle ϕ_i , the centre of the tool is $O(x_i, y_i)$, and the instantaneous position of the tool tip is $P = [x_{\text{tip}}(i, j, k), y_{\text{tip}}(i, j, k)]^T$. The intersection of the line PO and the trajectory of the previous m^{th} tooth (tooth index $k-m$) is $Q = [x_{\text{int}}(i, j, k-m), y_{\text{int}}(i, j, k-m)]^T$. The distance $d(i, j, k-m)$ between the tool tip P and the intersection point Q can be calculated by Eq. (4). It is worth noting that if the line PO between the tool tip P and the tool centre O does not intersect the previous tool trajectory, i.e., Q does not exist, meaning that no material is removed at this point, then the distance d is assigned 0. Alternatively, as the tool moves back and forth in UVAM, there may be multiple intersections between the line PO and the trajectory of the previous m^{th} tooth, i.e., Q is a row vector, then the distance $d(i, j, k-m)$ is equal to the minimum of all possible distances.

$$d(i, j, k - m) = \begin{cases} 0, & \text{if } Q \text{ does not exist} \\ \min \left[\sqrt{(x_{\text{tip}} - x_{\text{int}})^2 + (y_{\text{tip}} - y_{\text{int}})^2} \right], & \text{else} \end{cases} \quad (4)$$

Fig. 1 Schematic diagram of UVAM **a** 3D view and **b** cross-sectional view of tool

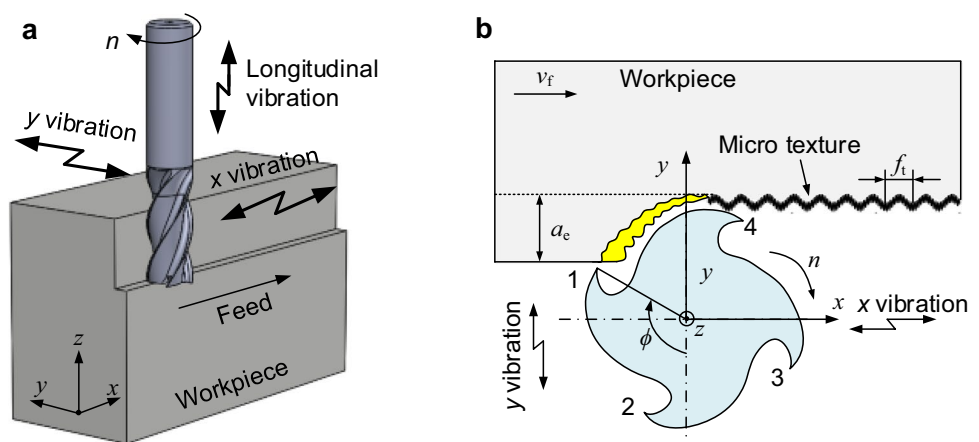
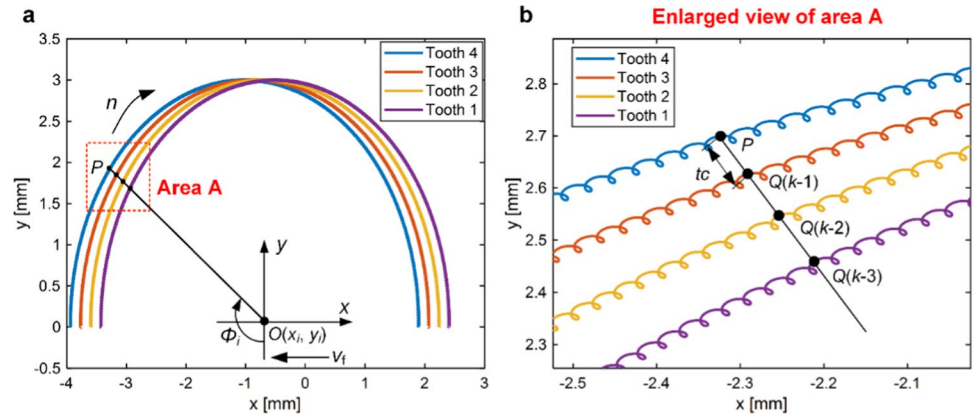


Fig. 2 **a** Tool trajectory in UVAM and **b** magnified view of area A



Due to tool runout or vibration, the tooth k does not necessarily remove the material left by the previous 1st tooth (tooth index $k - 1$), but may be by the previous m^{th} tooth [66]. Then, actual instantaneous cutting thickness $tc(i, j, k)$ is the minimum of all possible cutting thicknesses, as shown in Eq. (5):

$$tc(i, j, k) = \min[d(i, j, k - 1), d(i, j, k - 2), \dots, d(i, j, k - N_t)] \quad (5)$$

The instantaneous cutting thickness is calculated in MATLAB. As an example, Fig. 3 illustrates the comparison of cutting thickness in UVAM and CM, down-milling methods. It can be found that the instantaneous cutting thickness in UVAM oscillates at a high frequency in the nominal cutting thickness position.

Differentiating the displacement (Eq. (1)) to time, then the instantaneous cutting speed of tool tip is obtained as follows:

$$\begin{aligned} v_x &= -R\omega \cos(\omega t) - A_x \cdot 2\pi f \sin(2\pi f t + \theta_x) - v_t \\ v_y &= +R\omega \sin(\omega t) - A_y \cdot 2\pi f \sin(2\pi f t + \theta_y) \\ v_z &= -A_z \cdot 2\pi f \sin(2\pi f t + \theta_z) \end{aligned} \quad (6)$$

The cutting speeds in the x , y , and z directions are transformed to the tangential, normal, and axial directions:

$$\begin{pmatrix} v_t \\ v_r \\ v_a \end{pmatrix} = T \begin{pmatrix} v_x \\ v_y \\ v_z \end{pmatrix} = \begin{pmatrix} \cos\phi & -\sin\phi & 0 \\ \sin\phi & \cos\phi & 0 \\ 0 & 0 & -1 \end{pmatrix} \begin{pmatrix} v_x \\ v_y \\ v_z \end{pmatrix} \quad (7)$$

As an example, Fig. 4 presents the instantaneous tangential and radial cutting speeds in UVAM and CM. For CM, both the radial velocity v_r and the tangential velocity v_t remain approximately constant, being approximately equal to 0 and wR , respectively, whereas for UVAM, the amplitudes of the radial and tangential cutting speeds are substantially increased. According to Eq. (6), the amount of increase in speed amplitude depends on the product of ultrasonic vibration amplitude A and frequency f , $A \times 2\pi f$. Another function of UVAM is to separate tool-chip and tool-workpiece at a high frequency, as both v_t and v_r change their directions at a high frequency.

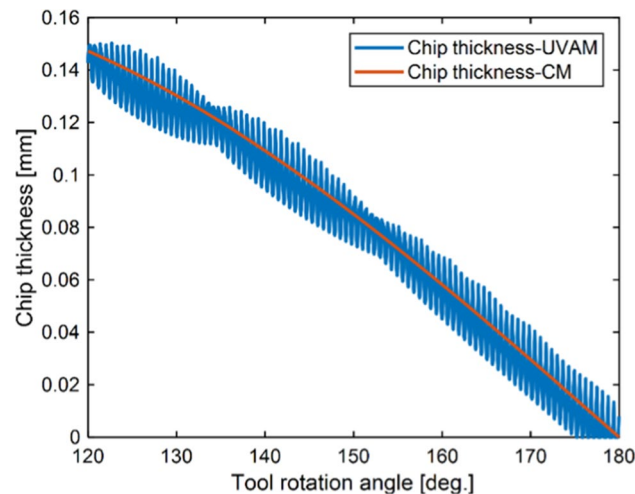


Fig. 3 Instantaneous cutting thickness in UVAM and CM

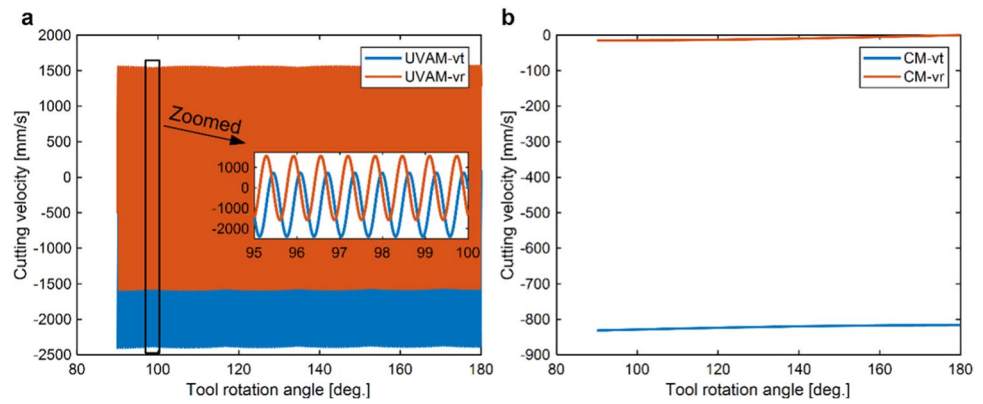
3 Surface roughness prediction model

In this section, the tool trajectory is first predicted in Section 3.1, where the effects of tool runout, tool vibration, and tool deflection on the trajectory are considered. Then, in Section 3.2, the material springback is calculated based on the instantaneous cutting thickness. Roughness parameters are then calculated in Section 3.3 based on the predicted surface profile.

3.1 Tool trajectory

Tool runout is almost inevitable during milling, which has a significant impact on surface topography as it changes the

Fig. 4 The instantaneous tangential v_t and radial v_r cutting speeds in **a** UVAM and **b** CM



instantaneous radius of each tooth. Figure 5 shows a diagram of tool runout with the cross-section being at the bottom of the milling cutter. Point O is the rotation center, and point O' is the geometric centre of tool; these two points do not coincide. The instantaneous radius of rotation of the tool as a function of tooth index and axial height is given by Eq. (8) [66]:

$$R_{j,k} = R + \rho \cos \left(\lambda - \frac{z_j \tan \beta}{R} - (k - 1)\phi_p \right) \quad (8)$$

where ρ is eccentricity distance and λ is eccentricity direction.

The tool deflection model is shown in Fig. 6. The end mill is modelled as a cantilever beam. The tool is deflected

by milling forces in both x and y directions. At time t_i , static deflections of the j^{th} axial slice can be calculated by the following equations:

$$\begin{aligned} x_d(z_j, t_i) &= \frac{1}{6EL} \left[\int_0^{z_j} q_x(L-z_j)^2(2L+z_j-3x)dx + \int_{z_j}^{z_j+q_x} q_x(L-x)^2(2L-3z_j+x)dx \right] \\ y_d(z_j, t_i) &= \frac{1}{6EL} \left[\int_0^{z_j} q_y(L-z_j)^2(2L+z_j-3y)dy + \int_{z_j}^{z_j+q_y} q_y(L-y)^2(2L-3z_j+y)dy \right] \end{aligned} \quad (9)$$

where x_d , I_x , and q_x are, respectively, deflection, moment of inertia, and load concentration in the x direction (feed direction). The same naming rules apply to the physical quantities in the y direction (vertical feed direction); l is clamping length of end mill.

The vibration displacements x_v and y_v of the tool in the x and y directions, respectively, can be obtained by solving the following second-order inhomogeneous linear differential equations:

$$\begin{aligned} \ddot{x}(t) + 2\zeta_x \omega_{nx} \dot{x}(t) + \omega_{nx}^2 x(t) &= \frac{\omega_{nx}^2}{k_x} F_x(t) \\ \ddot{y}(t) + 2\zeta_y \omega_{ny} \dot{y}(t) + \omega_{ny}^2 y(t) &= \frac{\omega_{ny}^2}{k_y} F_y(t) \end{aligned} \quad (10)$$

where ω_n is natural frequency, ζ is damping ratio, k is modal stiffness, and $F_x(t)$ and $F_y(t)$ are milling forces. $F_x(t)$ and $F_y(t)$ can be obtained by experimental measurements or analytical predictions [67, 68].

By substituting tool's actual radius of rotation (Eq. (8)), static tool deflections (Eq. (9)) and vibration displacements solved by Eq. (10) into ideal tool trajectories (Eq. (1)), the actual tool trajectories are expressed by:

$$\begin{aligned} x(i, j, k) &= -R_{j,k} \sin(\phi_{i,j,k}) + A_x \cos(2\pi ft + \theta_x) - v_t t + x_d(i, j) + x_v(i, j) \\ y(i, j, k) &= -R_{j,k} \cos(\phi_{i,j,k}) + A_y \cos(2\pi ft + \theta_y) + y_d(i, j) + y_v(i, j) \\ z(i, j, k) &= z_j + A_z \cos(2\pi ft + \theta_z) \end{aligned} \quad (11)$$

The surface topography is the result of interference between the trajectories of all cutter teeth all axial heights and the work-piece, and it can be reconstructed by performing interpolation and Boolean operation. If tool runout, deflection, and vibration are taken into account, the reconstructed surface topography model is also referred to as a geometric-kinematic-dynamic

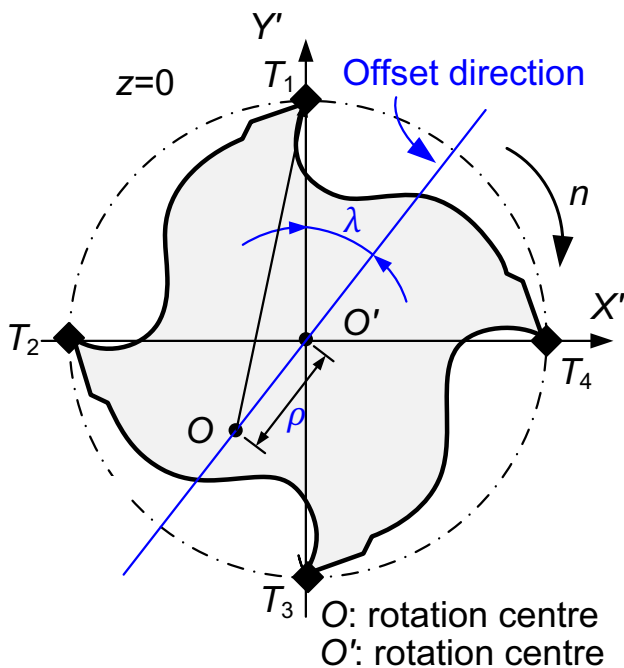


Fig. 5 Schematic diagram of tool runout

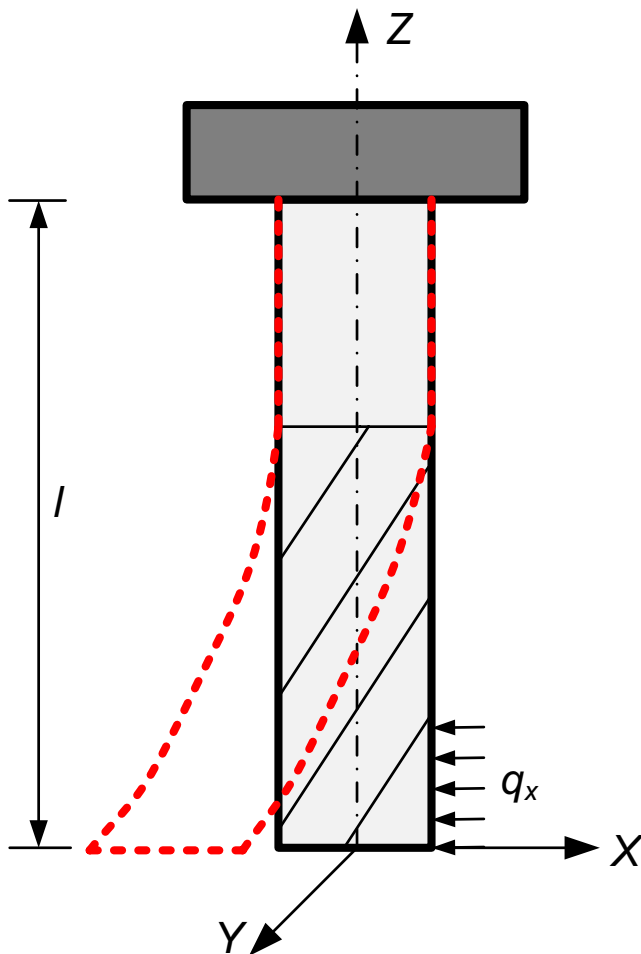


Fig. 6 Tool deflection model

model. Matrix $Y(j, i)$ represents the height of reconstructed geometric-kinematic-dynamic surface topography, with the column i representing the index of feed position (x direction, as shown in Fig. 1), the row j representing the index of axial position (z direction), and $Y(j, i)$ representing the surface height in feed position i and axial position j .

As an example, Fig. 7 (a) presents the simulated surface topography when only feed rate is considered in CM. Figures 7(b)–(e) show the simulated surface topography when different factors are considered in UVAM. It can be seen from Fig. 7(b) that, compared with CM, UVAM induces high-frequency vibration marks on the machined surface and increases the maximum height of surface profile. Tool runout (Fig. 7(c)), tool vibration (Fig. 7(d)), and tool deflection (Fig. 7(E)) further change the shape of surface topography in UVAM.

3.2 Material elastic recovery

For UVAM, the amplitude of ultrasonic vibration and the tool edge radius are close (in the micron range), so

it is essential to consider size effect during UVA cutting process. As Fig. 8 shows, since cutter edge is not absolutely sharp, and the material below the separation point O will not be removed as chip but will be squeezed by the tool flank face and subsequently elastically recovered. Thus, the effective cutting thickness h_{eff} is less than the nominal cutting thickness h_D . The height of the separation point O is the minimum cutting thickness h_{min} . If the nominal undeformed chip thickness h_D is less than h_{min} , no chips will be produced, and only ploughing and subsequent springback of the material will occur. h_{min} is given by [69]

$$h_{\text{min}} = C_r \cdot r_\beta \quad (12)$$

where c_r is an empirical constant and r_β is cutter edge radius.

While generating the tool tip trajectory (Eq. (11)), the instantaneous cutting thickness of all cutter teeth at all axial heights is also calculated based on the method described in Section 2. Then, the cutting thickness matrix tc corresponding to the geometric-kinematic-dynamic surface topography matrix Y is reconstructed. For example, for position (j, i) , the surface profile height is $Y(j, i)$ and the corresponding cutting thickness is $tc(j, i)$. It is worth noting that the reconstruction of matrix tc takes into account tool runout, tool vibration, and tool deflection. Considering material springback, then the geometric-kinematic-dynamic-physical surface topography matrix Y_s is formulated as

$$Y_s(j, i) = \begin{cases} Y(j, i) + h_{\text{min}}, & \text{if } tc(j, i) \geq h_{\text{min}} \\ Y(j, i) + tc(j, i), & \text{else} \end{cases} \quad (13)$$

3.3 Surface roughness parameters

Once the physical model of surface topography has been reconstructed, the roughness parameters can be calculated. The arithmetic mean deviation R_a of the profile is expressed as

$$R_a = \frac{1}{L} \int_0^L |y(x)| dx = \frac{1}{N} \sum_{i=1}^N |y_i - y_m| \quad (14)$$

where L is the sampling length, N is the number of sampling points, and y_m is the arithmetic mean centreline of the profile, which divides the profile into upper and lower parts with equal area. y_m is determined by

$$y_m = \frac{1}{N} \sum_{i=1}^N y_i \quad (15)$$

The maximum height R_z of the profile, i.e., the distance between the highest peak and the deepest valley within the sampling length, is determined by

Fig. 7 Simulated surface topography **a** considering feed only in CM, **b** considering feed only in UVAM, **c** considering feed and runout in UVAM, **d** considering feed, tool runout, and tool vibration in UVAM, and **e** considering feed, tool runout, tool vibration, and tool deflection in UVAM

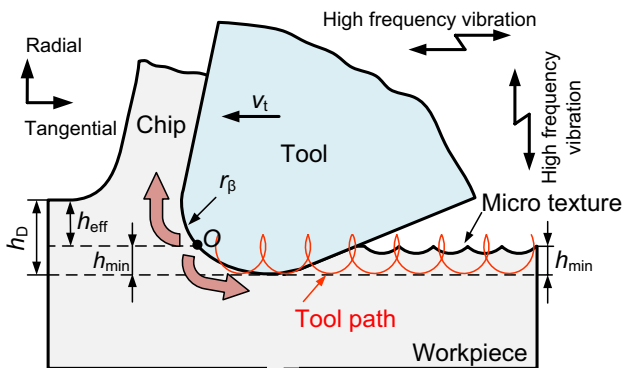
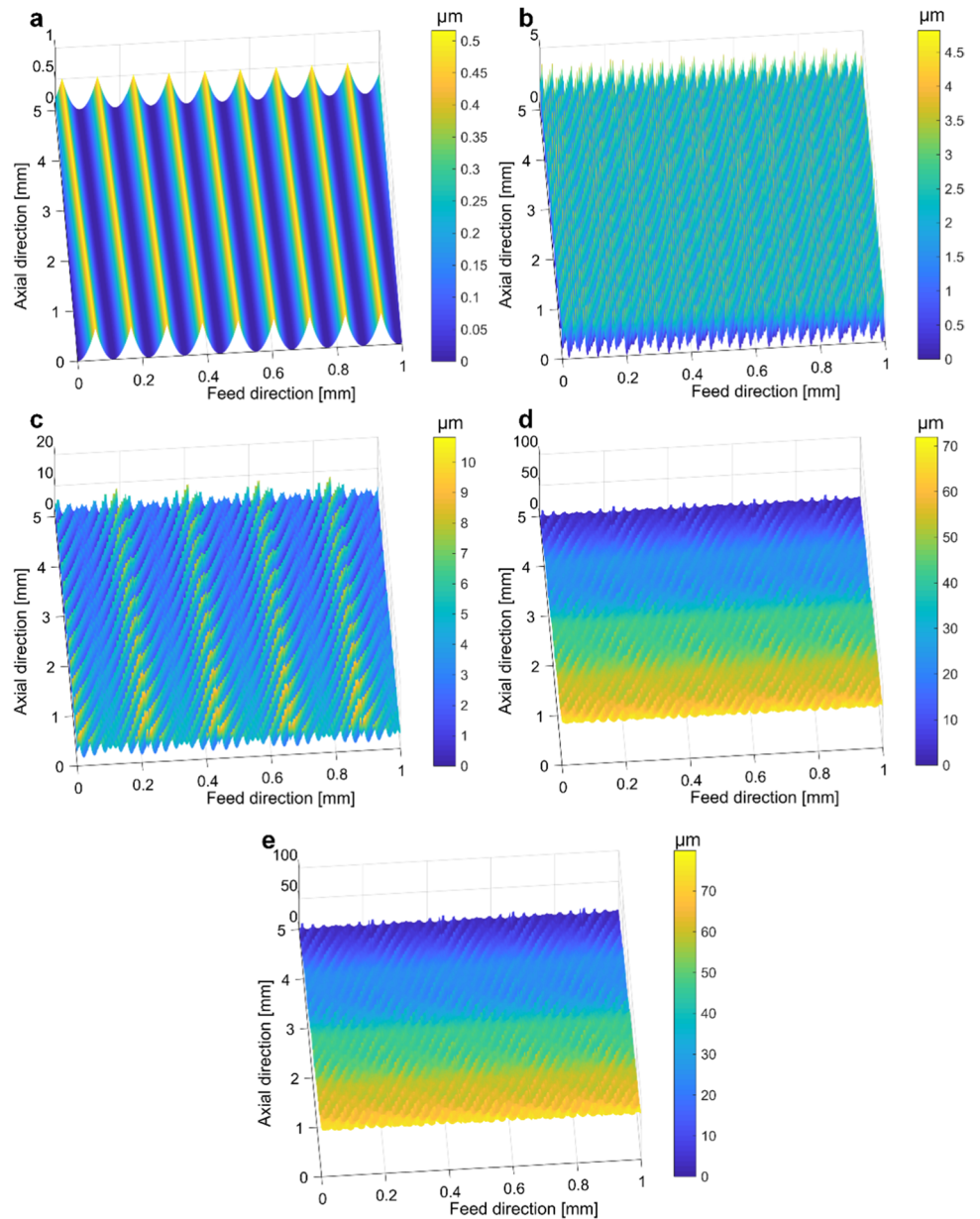


Fig. 8 Schematic diagram of material springback in UVA cutting process

$$R_z = \max_{i=1}^N (y_i - y_m) + \min_{i=1}^N (y_i - y_m) \quad (16)$$

4 Experiment

The experimental setup is illustrated in Fig. 9. The UVAM experiment was performed in a vertical CNC machining center HURCO VMX42. Side milling operation was adopted. The ultrasonic vibration system consisted of an ultrasonic generator, an ultrasonic transducer, and a horn. The ultrasonic generator served to increase the frequency of alternating current and to drive ultrasonic transducer. The ultrasonic transducer

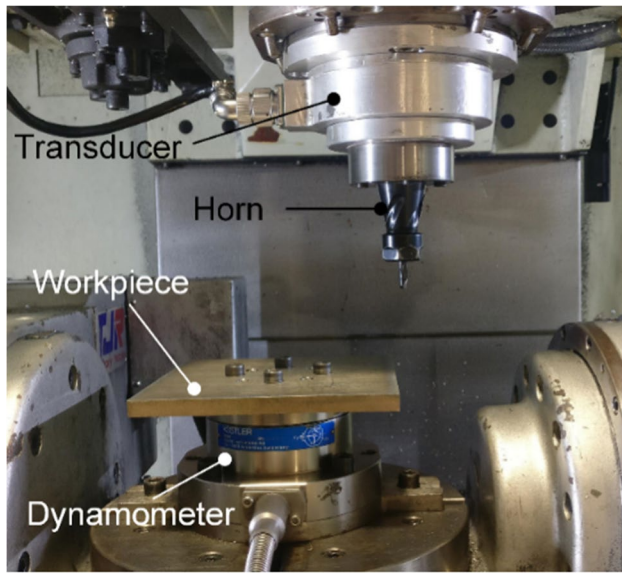


Fig. 9 Experimental setup

converted high-frequency alternating current into high-frequency mechanical vibrations. The horn amplified vibration amplitude produced by the ultrasonic transducer. The workpiece material was titanium alloy Ti–6Al–4 V. The workpiece and tool parameters are shown in Table 1. The modal parameters of end mill were obtained by impact hammer test, natural frequency $\omega_{nx} = 1515.7$ Hz, $\omega_{ny} = 1500.3$ Hz, damping ratio $\zeta_x = 4.1\%$, $\zeta_y = 3\%$, modal stiffness $k_x = 8.6 \times 10^6$ N/m, and $k_y = 6.3 \times 10^6$ N/m. The milling forces were measured by Kistler 9272 dynamometer equipped with Kistler 5070A charge amplifier. The sampling frequency of cutting forces was 100 kHz. The amplitude and frequency of ultrasonic vibration were measured by KEYENCE LK-H008W laser displacement sensor, $A_x = A_y = 1$ μ m, $A_z = 0.5$ μ m, $f = 20.64$ kHz, and $\theta_x = \theta_y = \theta_z = 0$. Table 2 presents the machining parameters. The feed per tooth f_t was taken as the independent variable, and 6 levels of f_t were set. Both UVAM and CM operations were conducted at various f_t . The milling length of each trial was very small, only 18 mm, to exclude the influence of tool wear on surface roughness. After milling experiments, surface morphology was analyzed using Keyence VHX-500 FE optical microscope. Surface roughness and surface profile were measured utilizing Mitutoyo SJ-210 Portable Surface Roughness Tester.

Table 1 Workpiece and tool parameters

Workpiece materials		Tool parameters				
Vickers hardness H_v	Elastic modulus E (GPa)	Tooth number	Diameter d (mm)	Helix angle β ($^\circ$)	Runout ρ (μ m)	Runout λ ($^\circ$)
349	113.8	2	6	30	28	95 $^\circ$

Table 2 Milling parameters

Experiment number	Cutting speed v_c (m/min)	Feed per tooth f_t (mm)	Radial depth of cut a_c (mm)	Axial depth of cut a_p (mm)	Cutting conditions
1–6	50	0.02, 0.05, 0.08, 0.11, 0.14, and 0.17	1.5	5	UVAM, CM

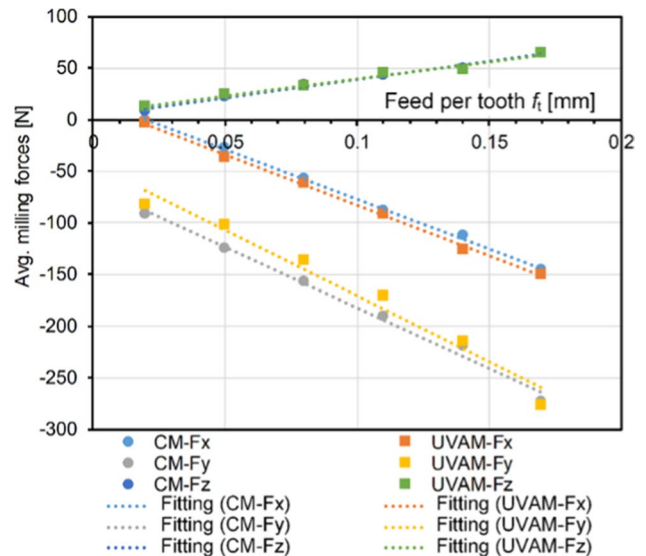


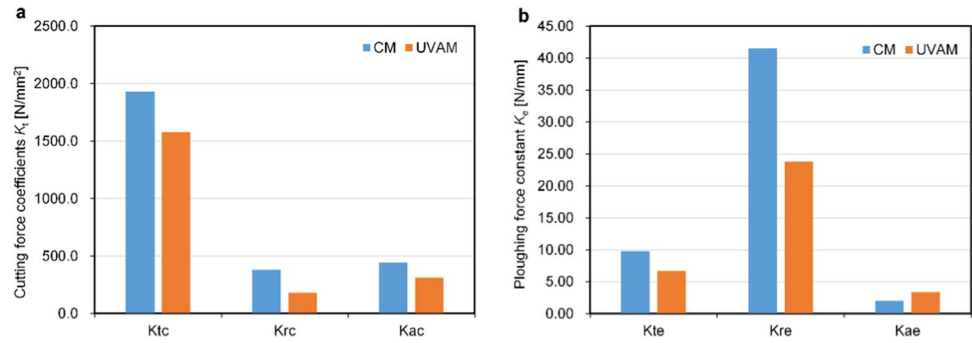
Fig. 10 Average values of F_x , F_y , and F_z and their linear regressions

5 Results and discussion

5.1 Average milling forces and milling force coefficients

According to the method proposed by Budak [70], linear regressions are performed on the average values of measured milling forces F_x , F_y , and F_z , as shown in Fig. 10, to calculate their ploughing force components and cutting force components. Then, the milling force coefficients are determined using the linear edge force model (Eq. (17), [70]). The cutting force components result from material’s shear deformation in the primary zone and tool-chip friction in the secondary zone,

Fig. 11 **a** K_{tc} , K_{rc} , and K_{ac} ; **b** K_{te} , K_{re} , and K_{ae}



while the ploughing force components result from ploughing effect of tool-workpiece interface in the tertiary zone:

$$\begin{aligned}
 dF_{tk}(\phi, z) &= [K_{te} + K_{tc}h_k(\phi, z)]dz \\
 dF_{rk}(\phi, z) &= [K_{re} + K_{rc}h_k(\phi, z)]dz \\
 dF_{ak}(\phi, z) &= [K_{ae} + K_{ac}h_k(\phi, z)]dz
 \end{aligned}
 \tag{17}$$

where K indicates milling force coefficients and dF indicates differential milling forces. The subscripts t, r, and a denote tangential, radial, and axial, respectively. K_c (in MPa) denotes cutting force coefficient, also known as specific cutting energy, which represents the cutting force component per unit area. K_e (in N/mm) denotes ploughing force coefficient, which represents the ploughing force per unit contact length. h_k is uncut chip thickness for tooth k .

It is worth noting that the dynamometer used in this experiment has a limited bandwidth (3 kHz); therefore,

the instantaneous milling forces are distorted due to the dynamometer-workpiece assembly dynamics [71]. However, Grossi et al. [72] have rigorously demonstrated that the dynamometer-workpiece assembly dynamics does not affect the average value of the milling force. Furthermore, Grossi et al. [72] have also shown that the calibration method of milling force coefficients using the average milling forces (i.e., the method of Fig. 10) is also not affected by the dynamometer-workpiece assembly dynamics. This is because the milling force coefficients are calculated from the average milling forces (i.e., the DC component of the dynamic milling forces) and the transfer function of the force measurement system has a magnitude of 1 at 0 Hz [72–78], so neither the average milling forces nor the milling force coefficients are affected by the dynamometer-workpiece assembly dynamics. As can be seen in Fig. 10, ultrasonic vibration exerts negligible effect on the average value of

Fig. 12 Milled Ti-6Al-4 V surface morphology in UVAM and CM when $f_t=0.02$ mm and $f_t=0.17$ mm

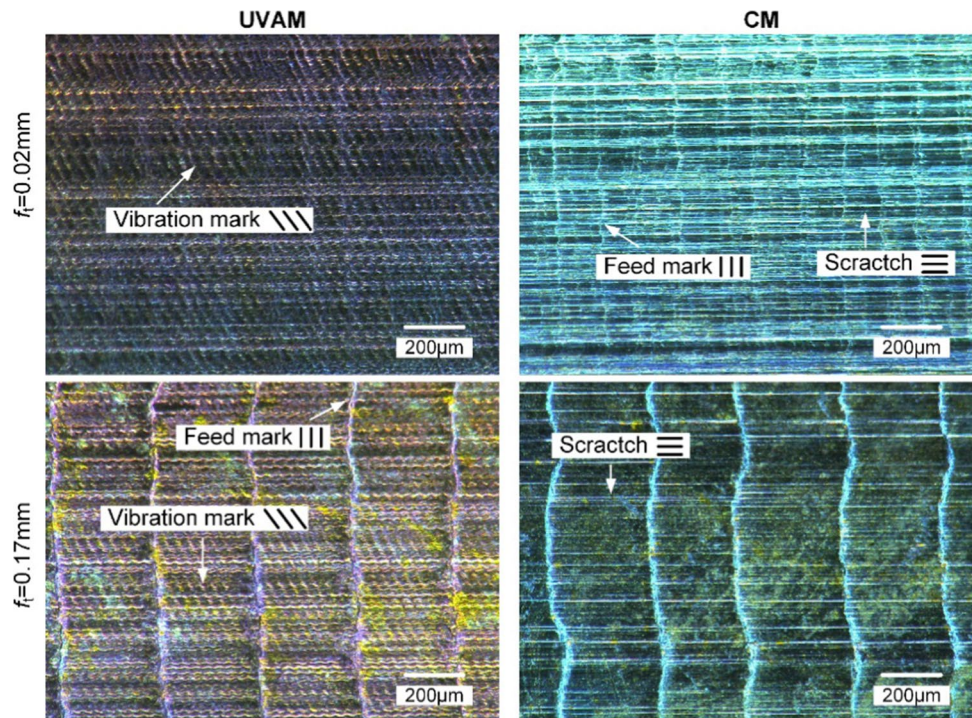
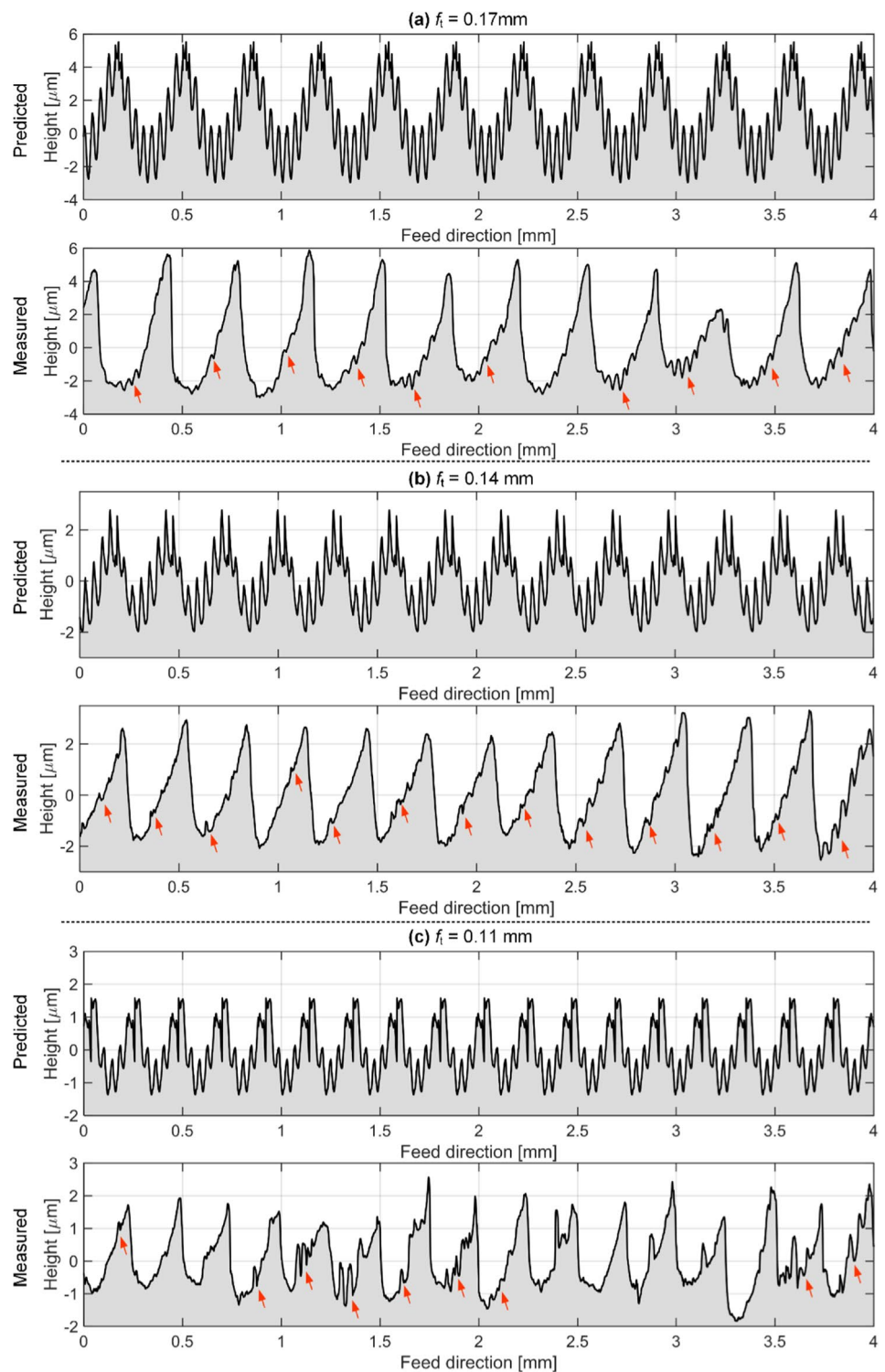


Fig. 13 Predicted and measured surface profiles in UVAM. **a** $f_t=0.17$ mm, **b** $f_t=0.14$ mm, and **c** $f_t=0.11$ mm (arrows point to ultrasonic vibration micro-textures)

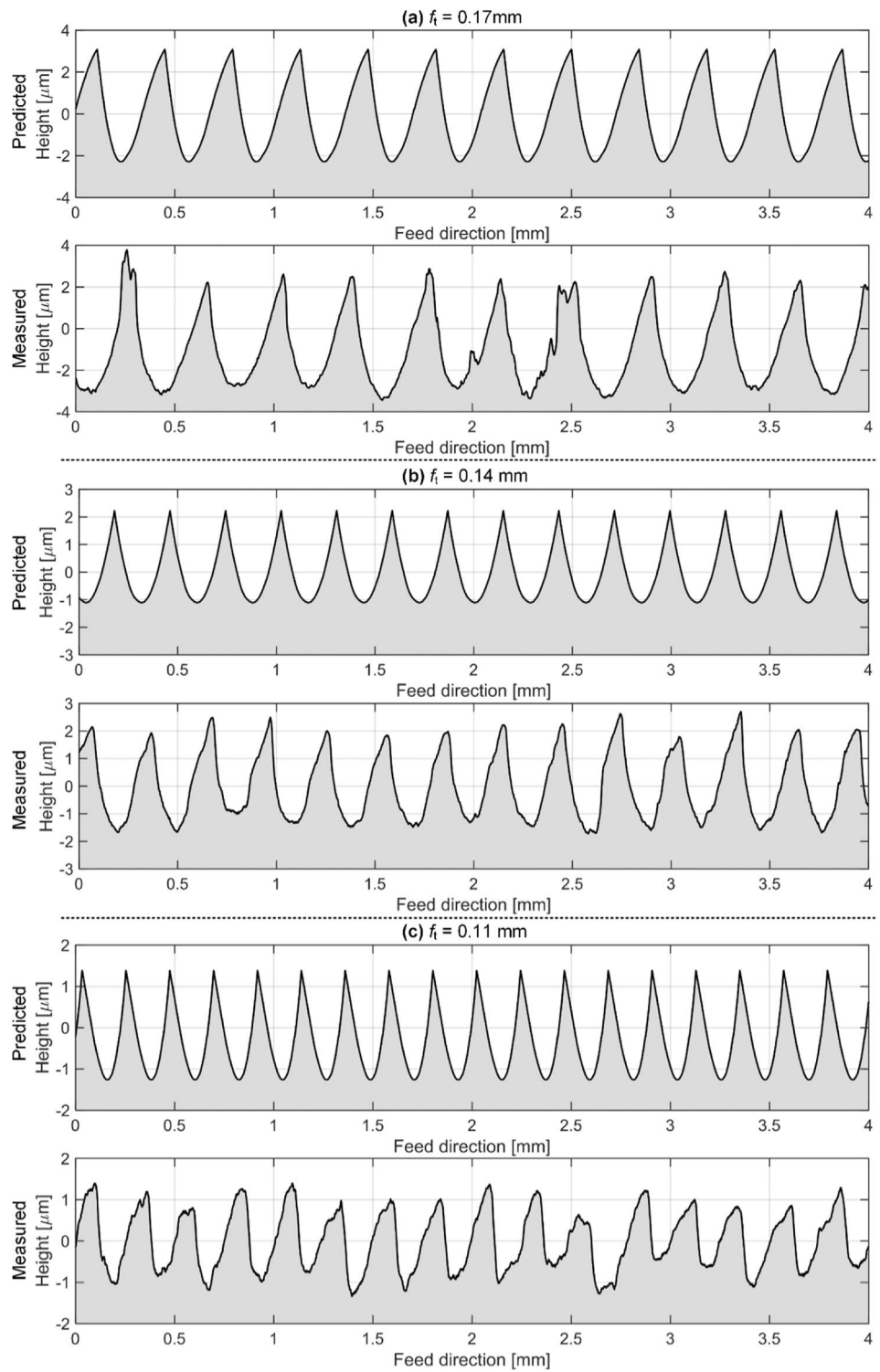


F_z . Besides, ultrasonic vibration increases the average value of F_x but reduces the average value of F_y . However, since both F_x and F_y are obtained by projective transformation of tangential F_t and radial F_r milling forces, in order to investigate the effect of ultrasonic vibration on cutting mechanism, it is necessary to compare the milling force coefficients in

UVAM and CM processes. Milling force coefficients reflect cutting mechanism better than F_x , F_y , and F_z , and the acquisition of them is a prerequisite for predicting milling forces for a given machining condition.

As shown in Fig. 11, ultrasonic vibration can significantly reduce cutting force coefficients. K_{tc} , K_{rc} , and K_{ac} in UVAM

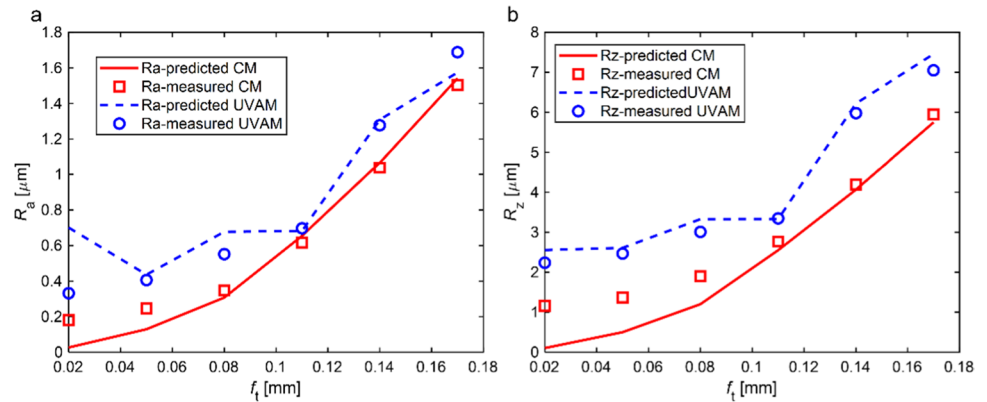
Fig. 14 Predicted and measured surface profiles in CM. **a** $f_t=0.17$ mm, **b** $f_t=0.14$ mm, and **c** $f_t=0.11$ mm



are reduced by -18.23 , -52.98 , and -29.74% , respectively, in comparison with CM. The reduction in cutting force coefficients is due to the high frequency separation of tool and chip induced by ultrasonic vibration. From the energy point of view, UVAM additionally provides an impact energy at the ultrasonic vibration frequency, which promotes material

removal. For the ploughing force coefficients, ultrasonic vibration reduces K_{te} and K_{re} by -32.16 and -42.77% , respectively, compared with CM. It signifies a weakening of ploughing in tool-workpiece interface in UVAM. This weakening is also accredited to the separation effect of tool-workpiece resulting from UVAM (see Fig. 4). However,

Fig. 15 Predicted and measured surface roughness parameters: **a** R_a and **b** R_z



axial ploughing constant K_{ac} is increased by 67.83%, which is attributed to the high-frequency relative motion and friction in axial direction between tool and workpiece caused by ultrasonic longitudinal vibration.

5.2 Surface morphology

As an example, Fig. 12 presents the optical microscope photographs of the machined Ti–6Al–4 V surface in UVAM and CM when $f_i = 0.02$ mm and $f_i = 0.17$ mm. For CM, the machined surface has axial feed grooves and abrasive scratches that are parallel to the feed direction. For UVAM, in addition to these characteristics, the surface also has high-frequency and oblique microtextures distributed in the feed grooves. The regular microtextures induced by ultrasonic vibration do not disrupt the feed marks.

5.3 Surface profile

As some examples, Fig. 13 presents the predicted and measured surface profiles in UVAM when $f_i = 0.17$ mm, $f_i = 0.14$ mm, and $f_i = 0.11$ mm, with the red arrows in the figure pointing to the measured ultrasonic vibration microtextures. Figure 14 presents the predicted and measured surface profiles in CM when $f_i = 0.17$ mm, $f_i = 0.14$ mm, and $f_i = 0.11$ mm. In the case of CM, the predicted profile agrees well with the measured one in terms of the amplitude or shape of the profile. In the case of UVAM, for the predicted surface profile, the high-frequency microtextures can be clearly seen distributed among the feed grooves. The spacing and depth of the feed grooves are in good agreement with the predicted ones. For the measured profile, although ultrasonic vibration patterns exist (where the arrows point), they are not as pronounced as the predicted ones. There are two reasons for this: (1) ultrasonic vibration tool holders cannot guarantee a constant amplitude and frequency when subjected to periodically varying milling force loads [79] and (2) the surface profile is measured using a mechanical contact profiler. The radius of the mechanical stylus is about 5 µm, which is

similar to the amplitude of ultrasonic vibration (1 µm). Due to the expansion effect of the mechanical stylus, the measured profile is smoother than the actual profile. This phenomenon has also been confirmed by Nieslony et al. [80].

5.4 Surface roughness

Figure 15 presents the predicted and measured surface roughness parameters, i.e., R_a and R_z , in UVAM and CM. R_a and R_z in UVAM are, on average, 26 and 39% larger than those in CM, respectively. This is because UVAM generates additional high-frequency ripples in the feed grooves, resulting in a more complex texture. The roughness prediction model can explain the greater roughness of UVAM than CM. In addition, the average prediction error for R_a and R_z is 23%, indicating that the model is reasonable.

6 Conclusions

In this paper, the machinability of Ti–6Al–4 V under UVAM and CM conditions was evaluated in terms of milling force coefficients, surface topography, and surface roughness, and a predictive model of surface roughness was developed. The following conclusions can be drawn:

- (1) The tangential v_t and radial v_r cutting velocities in UVAM change their direction at high frequency; besides, the amplitude of v_t and v_r in UVAM is $A \times 2\pi f$ higher than that in CM, indicating separation and impact effect of tool-chip and tool-workpiece interfaces.
- (2) The tangential and radial cutting force coefficients for UVAM are reduced by –18.23 and –52.98%, respectively, and the tangential and radial ploughing force coefficients are reduced by –32.16 and –42.77%, respectively, compared to CM, due to the high-frequency and high-speed separation and impact effect. However, ultrasonic longitudinal vibration increases

axial ploughing constant due to relative motion between tool and workpiece in axial direction.

- (3) For CM, milled Ti–6Al–4 V surface is characterized by axial feed grooves and abrasive scratches parallel to feed direction. For UVAM, in addition to the aforementioned features, there is also high-frequency oblique microtexture distributed in feed grooves, resulting in a more complex texture.
- (4) R_a and R_z in UVAM are, on average, 26 and 39% larger than those in CM, which is accredited to the presence of additional high-frequency ripples induced by ultrasonic vibration. The average prediction error of the established model is 23%, indicating that the model is reasonable.

Funding This work was financially supported by National Natural Science Foundation of China (Grant number: 92160206).

Declarations

Conflict of interest The authors declare no competing interests.

References

1. Yang Z, Zhu L, Zhang G, Ni C, Lin B (2020) Review of ultrasonic vibration-assisted machining in advanced materials. *Int J Mach Tools Manuf* 156:103594. <https://doi.org/10.1016/j.ijmactools.2020.103594>
2. Cao Y, Zhu Y, Ding W, Qiu Y, Wang L, Xu J (2022) Vibration coupling effects and machining behavior of ultrasonic vibration plate device for creep-feed grinding of Inconel 718 nickel-based superalloy. *Chin J Aeronaut* 35(2):332–345. <https://doi.org/10.1016/j.cja.2020.12.039>
3. Patil S, Joshi S, Tewari A, Joshi SS (2014) Modelling and simulation of effect of ultrasonic vibrations on machining of Ti6Al4V. *Ultrasonics* 54(2):694–705. <https://doi.org/10.1016/j.ultras.2013.09.010>
4. Li C, Zhang F, Meng B, Liu L, Rao X (2017) Material removal mechanism and grinding force modelling of ultrasonic vibration assisted grinding for SiC ceramics. *Ceram Int* 43(3):2981–2993. <https://doi.org/10.1016/j.ceramint.2016.11.066>
5. Xu W, Zhang LC, Wu Y (2014) Elliptic vibration-assisted cutting of fibre-reinforced polymer composites: understanding the material removal mechanisms. *Compos Sci Technol* 92:103–111. <https://doi.org/10.1016/j.compscitech.2013.12.011>
6. Wang H, Pei ZJ, Cong W (2020) A feeding-directional cutting force model for end surface grinding of CFRP composites using rotary ultrasonic machining with elliptical ultrasonic vibration. *Int J Mach Tools Manuf* 152:103540. <https://doi.org/10.1016/j.ijmactools.2020.103540>
7. Xu J, Feng P, Feng F, Zha H, Liang G (2021) Subsurface damage and burr improvements of aramid fiber reinforced plastics by using longitudinal-torsional ultrasonic vibration milling. *J Mater Process Technol* 297:117265. <https://doi.org/10.1016/j.jmatprotec.2021.117265>
8. Xu W, Zhang LC (2014) On the mechanics and material removal mechanisms of vibration-assisted cutting of unidirectional fibre-reinforced polymer composites. *Int J Mach Tools Manuf* 80–81:1–10. <https://doi.org/10.1016/j.ijmactools.2014.02.004>
9. Zhao B, Wu B, Yue Y, Ding W, Xu J, Guo G (2023) Developing a novel radial ultrasonic vibration-assisted grinding device and evaluating its performance in machining PTMCs. *Chin J Aeronaut*. <https://doi.org/10.1016/j.cja.2023.01.008>
10. Bai W, Roy A, Sun R, Silberschmidt VV (2019) Enhanced machinability of SiC-reinforced metal-matrix composite with hybrid turning. *J Mater Process Technol* 268:149–161. <https://doi.org/10.1016/j.jmatprotec.2019.01.017>
11. Dong Z, Zhang H, Kang R, Ran Y, Bao Y (2022) Mechanical modeling of ultrasonic vibration helical grinding of SiCf/SiC composites. *Int J Mech Sci* 234:107701. <https://doi.org/10.1016/j.ijmecsci.2022.107701>
12. Gao J, Altintas Y (2020) Chatter stability of synchronized elliptical vibration assisted milling. *CIRP J Manuf Sci Technol* 28:76–86. <https://doi.org/10.1016/j.cirpj.2019.11.006>
13. Ulutan D, Ozel T (2011) Machining induced surface integrity in titanium and nickel alloys: a review. *Int J Mach Tools Manuf* 51(3):250–280. <https://doi.org/10.1016/j.ijmactools.2010.11.003>
14. An Q, Cai C, Zou F, Liang X, Chen M (2020) Tool wear and machined surface characteristics in side milling Ti6Al4V under dry and supercritical CO₂ with MQL conditions. *Tribol Int* 151:106511. <https://doi.org/10.1016/j.triboint.2020.106511>
15. Cai C, Liang X, An Q, Tao Z, Ming W, Chen M (2021) Cooling/lubrication performance of dry and supercritical CO₂-based minimum quantity lubrication in peripheral milling Ti-6Al-4V. *Int J Pr Eng Man-GT* 8(2):405–421. <https://doi.org/10.1007/s40684-020-00194-7>
16. Liu D, Li C, Dong L, Qin A, Zhang Y, Yang M, Gao T, Wang X, Liu M, Cui X, Ali HM, Sharma S (2022) Kinematics and improved surface roughness model in milling. *Int J Adv Manuf Technol*. <https://doi.org/10.1007/s00170-022-10729-8>
17. Wu P, Dai H, Li Y, He Y, Zhong R, He J (2022) A physics-informed machine learning model for surface roughness prediction in milling operations. *Int J Adv Manuf Technol* 123(11):4065–4076. <https://doi.org/10.1007/s00170-022-10470-2>
18. Verma GC, Pandey PM (2019) Machining forces in ultrasonic-vibration assisted end milling. *Ultrasonics* 94:350–363. <https://doi.org/10.1016/j.ultras.2018.07.004>
19. Cao Y, Ding W, Zhao B, Wen X, Li S, Wang J (2022) Effect of intermittent cutting behavior on the ultrasonic vibration-assisted grinding performance of Inconel 718 nickel-based superalloy. *Precis Eng* 78:248–260. <https://doi.org/10.1016/j.precisioneng.2022.08.006>
20. Gao G, Xia Z, Yuan Z, Xiang D, Zhao B (2020) Influence of longitudinal-torsional ultrasonic-assisted vibration on micro-hole drilling Ti-6Al-4V. *Chin J Aeronaut*. <https://doi.org/10.1016/j.cja.2020.06.012>
21. Liu X, Wang W, Jiang R, Xiong Y, Lin K, Li J, Shan C (2020) Analytical model of cutting force in axial ultrasonic vibration-assisted milling in-situ TiB₂/7050Al PRMMCs. *Chin J Aeronaut*. <https://doi.org/10.1016/j.cja.2020.08.009>
22. Feng Y, Hsu F-C, Lu Y-T, Lin Y-F, Lin C-T, Lin C-F, Lu Y-C, Liang SY (2020) Temperature prediction of ultrasonic vibration-assisted milling. *Ultrasonics* 108:106212. <https://doi.org/10.1016/j.ultras.2020.106212>
23. Peng Z, Zhang X, Zhang D (2021) Effect of radial high-speed ultrasonic vibration cutting on machining performance during finish turning of hardened steel. *Ultrasonics* 111:106340. <https://doi.org/10.1016/j.ultras.2020.106340>
24. Ni C, Zhu L, Liu C, Yang Z (2018) Analytical modeling of tool-workpiece contact rate and experimental study in ultrasonic vibration-assisted milling of Ti–6Al–4V. *Int J Mech Sci* 142–143:97–111. <https://doi.org/10.1016/j.ijmecsci.2018.04.037>

25. Jung H, Hayasaka T, Shamoto E, Xu L (2020) Suppression of forced vibration due to chip segmentation in ultrasonic elliptical vibration cutting of titanium alloy Ti–6Al–4V. *Precis Eng* 64:98–107. <https://doi.org/10.1016/j.precisioneng.2020.03.017>
26. Lotfi M, Charkhian A, Akbari J (2022) Surface analysis in rotary ultrasonic-assisted milling of CFRP and titanium. *J Manuf Process* 84:174–182. <https://doi.org/10.1016/j.jmapro.2022.10.006>
27. Greco S, Klauer K, Kirsch B, Aurich JC (2021) Vibration-assisted micro milling of AISI 316L produced by laser-based powder bed fusion. *J Manuf Process* 71:298–305. <https://doi.org/10.1016/j.jmapro.2021.09.020>
28. Cao Y, Yin J, Ding W, Xu J (2021) Alumina abrasive wheel wear in ultrasonic vibration-assisted creep-feed grinding of Inconel 718 nickel-based superalloy. *J Mater Process Technol* 297:117241. <https://doi.org/10.1016/j.jmatprotec.2021.117241>
29. Sorgato M, Bertolini R, Ghiotti A, Bruschi S (2021) Tool wear analysis in high-frequency vibration-assisted drilling of additive manufactured Ti6Al4V alloy. *Wear* 477:203814. <https://doi.org/10.1016/j.wear.2021.203814>
30. Ni C, Zhu L (2020) Investigation on machining characteristics of TC4 alloy by simultaneous application of ultrasonic vibration assisted milling (UVAM) and economical-environmental MQL technology. *J Mater Process Technol* 278:116518. <https://doi.org/10.1016/j.jmatprotec.2019.116518>
31. Namlu RH, Yılmaz OD, Lotfisadigh B, Kılıç SE (2022) An experimental study on surface quality of Al6061-T6 in ultrasonic vibration-assisted milling with minimum quantity lubrication. *Procedia CIRP* 108:311–316. <https://doi.org/10.1016/j.procir.2022.04.071>
32. Gao T, Zhang X, Li C, Zhang Y, Yang M, Jia D, Ji H, Zhao Y, Li R, Yao P, Zhu L (2020) Surface morphology evaluation of multi-angle 2D ultrasonic vibration integrated with nanofluid minimum quantity lubrication grinding. *J Manuf Process* 51:44–61. <https://doi.org/10.1016/j.jmapro.2020.01.024>
33. Sajjadi SA, Nouri Hossein Abadi H, Amini S, Nosouhi R (2016) Analytical and experimental study of topography of surface texture in ultrasonic vibration assisted turning. *Mater Des* 93:311–323. <https://doi.org/10.1016/j.matdes.2015.12.119>
34. Amini S, Hosseinabadi HN, Sajjadi SA (2016) Experimental study on effect of micro textured surfaces generated by ultrasonic vibration assisted face turning on friction and wear performance. *Appl Surf Sci* 390:633–648. <https://doi.org/10.1016/j.apsusc.2016.07.064>
35. Bertolini R, Ghiotti A, Bruschi S (2021) Wear behavior of Ti6Al4V surfaces functionalized through ultrasonic vibration turning. *J Mater Eng Perform* 30(10):7597–7608. <https://doi.org/10.1007/s11665-021-05952-5>
36. Börner R, Winkler S, Junge T, Titsch C, Schubert A, Drossel W-G (2018) Generation of functional surfaces by using a simulation tool for surface prediction and micro structuring of cold-working steel with ultrasonic vibration assisted face milling. *J Mater Process Technol* 255:749–759. <https://doi.org/10.1016/j.jmatprotec.2018.01.027>
37. Chen W, Zheng L, Xie W, Yang K, Huo D (2019) Modelling and experimental investigation on textured surface generation in vibration-assisted micro-milling. *J Mater Process Technol* 266:339–350. <https://doi.org/10.1016/j.jmatprotec.2018.11.011>
38. Chen P, Tong J, Zhao J, Zhang Z, Zhao B (2020) A study of the surface microstructure and tool wear of titanium alloys after ultrasonic longitudinal-torsional milling. *J Manuf Process* 53:1–11. <https://doi.org/10.1016/j.jmapro.2020.01.040>
39. Zhao B, Li P, Zhao C, Wang X (2020) Fractal characterization of surface microtexture of Ti6Al4V subjected to ultrasonic vibration assisted milling. *Ultrasonics* 102:106052. <https://doi.org/10.1016/j.ultras.2019.106052>
40. Xie W, Wang X, Zhao B, Li G, Xie Z (2022) Surface and subsurface analysis of TC18 titanium alloy subject to longitudinal-torsional ultrasonic vibration-assisted end milling. *J Alloys Compd* 929:167259. <https://doi.org/10.1016/j.jallcom.2022.167259>
41. Zhang M, Zhang D, Geng D, Liu J, Shao Z, Jiang X (2020) Surface and sub-surface analysis of rotary ultrasonic elliptical end milling of Ti-6Al-4V. *Mater Des* 191:108658. <https://doi.org/10.1016/j.matdes.2020.108658>
42. Maurotto A, Wickramarachchi CT (2016) Experimental investigations on effects of frequency in ultrasonically-assisted end-milling of AISI 316L: a feasibility study. *Ultrasonics* 65:113–120. <https://doi.org/10.1016/j.ultras.2015.10.012>
43. Krüger M, Denkena B (2013) Model-based identification of tool runout in end milling and estimation of surface roughness from measured cutting forces. *Int J Adv Manuf Technol* 65(5):1067–1080. <https://doi.org/10.1007/s00170-012-4240-y>
44. Buj-Corral I, Vivancos-Calvet J, González-Rojas H (2011) Influence of feed, eccentricity and helix angle on topography obtained in side milling processes. *Int J Mach Tools Manuf* 51(12):889–897. <https://doi.org/10.1016/j.ijmactools.2011.08.001>
45. Zhang X, Zhang W, Zhang J, Pang B, Zhao W (2017) Systematic study of the prediction methods for machined surface topography and form error during milling process with flat-end cutter. *P I Mech Eng B-J Eng* 233:095440541774092. <https://doi.org/10.1177/0954405417740924>
46. Lee KY, Kang MC, Jeong YH, Lee DW, Kim JS (2001) Simulation of surface roughness and profile in high-speed end milling. *J Mater Process Technol* 113(1):410–415. [https://doi.org/10.1016/S0924-0136\(01\)00697-5](https://doi.org/10.1016/S0924-0136(01)00697-5)
47. Wojciechowski S, Twardowski P, Pelic M, Maruda RW, Barrans S, Krolczyk GM (2016) Precision surface characterization for finish cylindrical milling with dynamic tool displacements model. *Precis Eng* 46:158–165. <https://doi.org/10.1016/j.precisioneng.2016.04.010>
48. Denkena B, Krüger M, Bachrathy D, Stepan G (2012) Model based reconstruction of milled surface topography from measured cutting forces. *Int J Mach Tools Manuf* 54–55:25–33. <https://doi.org/10.1016/j.ijmactools.2011.12.007>
49. Elbestawi MA, Ismail F, Yuen KM (1994) Surface topography characterization in finish milling. *Int J Mach Tools Manuf* 34(2):245–255. [https://doi.org/10.1016/0890-6955\(94\)90104-X](https://doi.org/10.1016/0890-6955(94)90104-X)
50. Yang D, Liu Z (2015) Surface plastic deformation and surface topography prediction in peripheral milling with variable pitch end mill. *Int J Mach Tools Manuf* 91:43–53. <https://doi.org/10.1016/j.ijmactools.2014.11.009>
51. Stepan G, Toth M, Bachrathy D, Ganeriwala S (2016) Spectral properties of milling and machined surface. *Mater Sci Forum* 836–837:570–577. <https://doi.org/10.4028/www.scientific.net/MSF.836-837.570>
52. Seguy S, Dessein G, Arnaud L (2008) Surface roughness variation of thin wall milling, related to modal interactions. *Int J Mach Tools Manuf* 48(3):261–274. <https://doi.org/10.1016/j.ijmactools.2007.09.005>
53. Grossi N, Scippa A, Sallèse L, Montevecchi F, Campatelli G (2018) On the generation of chatter marks in peripheral milling: a spectral interpretation. *Int J Mach Tools Manuf* 133:31–46. <https://doi.org/10.1016/j.ijmactools.2018.05.008>
54. Ismail F, Elbestawi MA, Du R, Urbasik K (1993) Generation of milled surfaces including tool dynamics and wear. *J Eng Ind* 115(3):245–252. <https://doi.org/10.1115/1.2901656>
55. Omar OEEK, El-Wardany T, Ng E, Elbestawi MA (2007) An improved cutting force and surface topography prediction model in end milling. *Int J Mach Tools Manuf* 47(7):1263–1275. <https://doi.org/10.1016/j.ijmactools.2006.08.021>
56. Morelli L, Grossi N, Campatelli G, Scippa A (2022) Surface location error prediction in 2.5-axis peripheral milling considering

- tool dynamic stiffness variation. *Precis Eng* 76:95–109. <https://doi.org/10.1016/j.precisioneng.2022.03.008>
57. Liu X, DeVor RE, Kapoor SG (2006) Model-based analysis of the surface generation in microendmilling—part I: Model Development. *J Manuf Sci E-T ASME* 129(3):453–460. <https://doi.org/10.1115/1.2716705>
 58. Arizmendi M, Fernández J, Gil A, Veiga F (2009) Effect of tool setting error on the topography of surfaces machined by peripheral milling. *Int J Mach Tools Manuf* 49(1):36–52. <https://doi.org/10.1016/j.ijmachtools.2008.08.004>
 59. Arizmendi M, Fernández J, Gil A, Veiga F (2010) Identification of tool parallel axis offset through the analysis of the topography of surfaces machined by peripheral milling. *Int J Mach Tools Manuf* 50(12):1097–1114. <https://doi.org/10.1016/j.ijmachtools.2010.07.006>
 60. Arizmendi M, Fernández J, Gil A, Veiga F (2010) Model for the prediction of heterogeneity bands in the topography of surfaces machined by peripheral milling considering tool runout. *Int J Mach Tools Manuf* 50(1):51–64. <https://doi.org/10.1016/j.ijmachtools.2009.09.007>
 61. Niu J, Jia J, Sun Y, Guo D (2020) Generation mechanism and quality of milling surface profile for variable pitch tools considering runout. *J Manuf Sci E-T ASME* 142(12). <https://doi.org/10.1115/1.4047622>
 62. Artetxe E, Olvera D, López de Lacalle LN, Campa FJ, Olvera D, Lamikiz A (2017) Solid subtraction model for the surface topography prediction in flank milling of thin-walled integral blade rotors (IBRs). *Int J Adv Manuf Technol* 90(1):741–752. <https://doi.org/10.1007/s00170-016-9435-1>
 63. Urbikain G, López de Lacalle LN (2018) Modelling of surface roughness in inclined milling operations with circle-segment end mills. *Simul Model Pract Theory* 84:161–176. <https://doi.org/10.1016/j.simpat.2018.02.003>
 64. Urbikain Pelayo G (2019) Modelling of static and dynamic milling forces in inclined operations with circle-segment end mills. *Precis Eng* 56:123–135. <https://doi.org/10.1016/j.precisioneng.2018.11.007>
 65. Urbikain Pelayo G, Olvera-Trejo D, Luo M, López de Lacalle LN, Elías-Zuñiga A (2021) Surface roughness prediction with new barrel-shape mills considering runout: Modelling and validation. *Measurement* 173:108670. <https://doi.org/10.1016/j.measurement.2020.108670>
 66. Kline WA, DeVor RE (1983) The effect of runout on cutting geometry and forces in end milling. *Int J Mach Tool Des Res* 23(2):123–140. [https://doi.org/10.1016/0020-7357\(83\)90012-4](https://doi.org/10.1016/0020-7357(83)90012-4)
 67. Altintas Y (2012) *Manufacturing automation: metal cutting mechanics, machine tool vibrations, and CNC design*, 2nd edn. Cambridge University Press, Cambridge
 68. Schmitz TL, Smith KS (2019) *Milling Dynamics. Machining dynamics: frequency response to improved productivity*. Cham: Springer International Publishing, 129–212
 69. Zong WJ, Huang YH, Zhang YL, Sun T (2014) Conservation law of surface roughness in single point diamond turning. *Int J Mach Tools Manuf* 84:58–63. <https://doi.org/10.1016/j.ijmachtools.2014.04.006>
 70. Budak E (2006) Analytical models for high performance milling. Part I: cutting forces, structural deformations and tolerance integrity. *Int J Mach Tools Manuf* 46(12):1478–1488. <https://doi.org/10.1016/j.ijmachtools.2005.09.009>
 71. Zhang X, Sui H, Zhang D, Jiang X (2018) Measurement of ultrasonic-frequency repetitive impulse cutting force signal. *Measurement* 129:653–663. <https://doi.org/10.1016/j.measurement.2018.06.043>
 72. Grossi N, Sallese L, Scippa A, Campatelli G (2015) Speed-varying cutting force coefficient identification in milling. *Precis Eng* 42:321–334. <https://doi.org/10.1016/j.precisioneng.2015.04.006>
 73. Kiran K, Kayacan MC (2019) Cutting force modeling and accurate measurement in milling of flexible workpieces. *Mech Syst Signal Process* 133:106284. <https://doi.org/10.1016/j.ymsp.2019.106284>
 74. Magnevall M, Lundblad M, Ahlin K, Broman G (2012) High frequency measurements of cutting forces in milling by inverse filtering. *Mach Sci Technol* 16(4):487–500. <https://doi.org/10.1080/10910344.2012.698970>
 75. Rubeo MA, Schmitz TL (2016) Mechanistic force model coefficients: a comparison of linear regression and nonlinear optimization. *Precis Eng* 45:311–321. <https://doi.org/10.1016/j.precisioneng.2016.03.008>
 76. Scippa A, Sallese L, Grossi N, Campatelli G (2015) Improved dynamic compensation for accurate cutting force measurements in milling applications. *Mech Syst Signal Process* 54–55:314–324. <https://doi.org/10.1016/j.ymsp.2014.08.019>
 77. Wan M, Yin W, Zhang W-H, Liu H (2017) Improved inverse filter for the correction of distorted measured cutting forces. *Int J Mech Sci* 120:276–285. <https://doi.org/10.1016/j.ijmecsci.2016.11.033>
 78. Totis G, Sortino M (2022) Upgraded regularized deconvolution of complex dynamometer dynamics for an improved correction of cutting forces in milling. *Mech Syst Signal Process* 166:108412. <https://doi.org/10.1016/j.ymsp.2021.108412>
 79. Zhao B, Bie W, Wang X, Chen F, Wang Y, Chang B (2019) The effects of thermo-mechanical load on the vibrational characteristics of ultrasonic vibration system. *Ultrasonics* 98:7–14. <https://doi.org/10.1016/j.ultras.2019.05.005>
 80. Nieslony P, Krolczyk GM, Zak K, Maruda RW, Legutko S (2017) Comparative assessment of the mechanical and electromagnetic surfaces of explosively clad Ti–steel plates after drilling process. *Precis Eng* 47:104–110. <https://doi.org/10.1016/j.precisioneng.2016.07.011>

Publisher's note Springer Nature remains neutral with regard to jurisdictional claims in published maps and institutional affiliations.

Springer Nature or its licensor (e.g. a society or other partner) holds exclusive rights to this article under a publishing agreement with the author(s) or other rightsholder(s); author self-archiving of the accepted manuscript version of this article is solely governed by the terms of such publishing agreement and applicable law.